Sailellah and Fukushima
Earth, Planets and Space (2023) 75:18
https://doi.org/10.1186/s40623-023-01773-z

Earth, Planets and Space

FULL PAPER

Open Access

Comparison of tropospheric delay correction methods for InSAR analysis using a mesoscale meteorological model: a case study from Japan

Sardila Nurulhikmah Sailellah[1*] and Yo Fukushima[2]

Abstract

A major source of error in interferometric synthetic aperture radar (InSAR), used for mapping ground deformation, is the delay caused by changes in the propagation velocity of radar microwaves in the troposphere. Correcting this tropospheric delay noise using numerical weather models is common because of their global availability. Various correction methods and tools exist; selecting the most appropriate one by considering weather models, delay models, and delay calculation algorithms is essential for specific applications. We compared the performance of two tropospheric delay correction methods applied to Advanced Land Observing Satellite-2 (ALOS-2) data acquired over Japan, where the atmospheric field is complex with significant seasonal variation. We tested: (1) a method of delay integration along the slant radar line-of-sight (LOS) path using the mesoscale model (MSM) provided by the Japan Meteorological Agency and (2) the Generic Atmospheric Correction Online Service (GACOS) for InSAR, which estimates delay using the high-resolution forecast (HRES)-European Centre for Medium-Range Weather Forecasts (ECMWF) products along with an iterative decomposition approach. The results showed that the tropospheric delay correction using the slant-delay integration approach with MSM, which has a finer temporal and spatial resolution, performed slightly better than GACOS. We further found that the differences in the refractivity models would have limited significance, suggesting that the difference in performance mainly originates from differences in the numerical weather models being used. This study highlights the importance of using the best-available numerical weather model data for tropospheric delay calculations.

Keywords Atmospheric delay, Tropospheric delay, Interferometric synthetic aperture radar, ALOS-2

*Correspondence:
Sardila Nurulhikmah Sailellah
sardila.sailellah@dc.tohoku.ac.jp
Full list of author information is available at the end of the article

Graphical Abstract

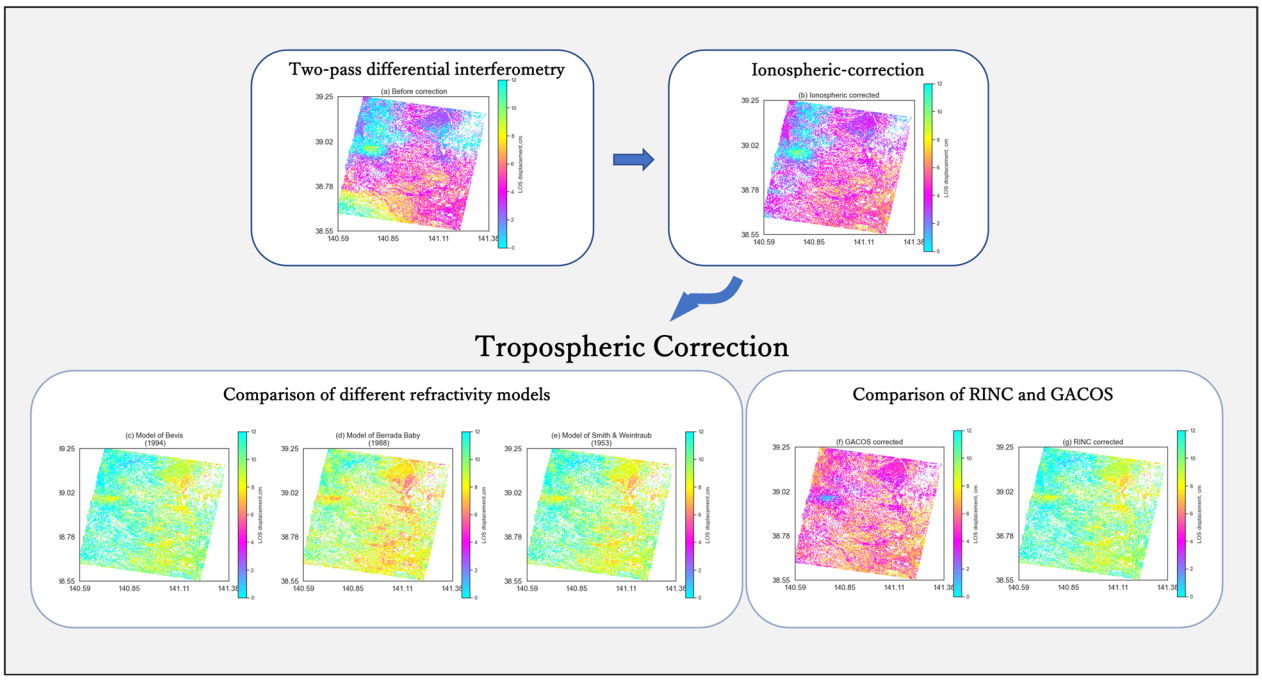

Introduction

Satellite-based interferometric synthetic aperture radar (InSAR) provides millimeter-scale measurements of ground surface deformation that can be used to identify surface deformations as well as their temporal variations on land (Massonnet et al. 1993; Bürgmann et al. 2000; Ferretti et al. 2001; Lanari et al. 2004; Colesanti and Wasowski 2006), sub-surface tectonic and anthropogenic processes such as fluid extraction and injection (Bekaert et al. 2017; Campbell et al. 2018; Murray and Lohman 2018), earthquakes, fault modeling (Hamiel and Fialko 2007; Xu and Zhu 2019; Ghayournajarkar and Fukushima 2020; Fukushima and Ishimura 2020), and volcanic inflation and deflation (Hooper et al. 2004, 2007; Gong et al. 2011), among others.

The phase of each pixel of an interferogram is a function of several factors, including surface displacement, orbital geometry of the satellite, topography, delay of the microwave in the atmosphere, and other noise (Massonnet and Feigl 1998). The topographic contributions are accounted for using the digital elevation model (DEM) (Massonnet and Feigl 1998). The orbital inaccuracy creates ramp-type artifacts, which can be corrected by simply removing the ramp assuming a polynomial function or using the long-wavelength displacement field measured by a GNSS network (Bekaert et al. 2016; Takada et al. 2018). Atmospheric delays remain as a major source of errors in InSAR because of the difficulty associated with their correction. Moreover, they often exhibit patterns similar to those due to earthquakes, volcanic activities, and land subsidence, limiting the signal detectability of InSAR (Zebker et al. 1997; Jolivet et al. 2014).

The propagation velocity of microwaves changes as the refractivity varies within the ionosphere and troposphere layers. In the ionospheric layer, the free electron density fluctuations in the ionized atmosphere alter the refractivity. The free electrons interact with electromagnetic waves as a dispersive medium, with inverse effects on the phase and group velocities with stronger effects at lower frequencies such as L-Band ALOS-2 data (Meyer et al. 2006; Wegmüller et al. 2006; Pi et al. 2011). In the tropospheric layer, fluctuations in the temperature, dry pressure, and water vapor pressure alter the refractivity. Tropospheric delay is typically divided into two components based on the physical origin, stratified and turbulent components. Stratified components are highly correlated with topography, affecting mountainous regions. Turbulent components are caused by disturbance processes in the troposphere. The tropospheric delay appears as a function of the refractivity along the path between the satellite and the ground (Shehaj et al. 2020). The state of the atmosphere is generally different

at the times when the two images used in InSAR processing are obtained. Consequently, a difference in the amount of delay appears in the interferogram, unrelated to the deformation.

Numerous studies have focused on mitigating tropospheric delay noise using various approaches. The first approach does not use external data; when multiple interferograms are available, noise can be mitigated by stacking or temporal filtering of the InSAR time series to separate tropospheric delay noise from the deformation signal (Ferretti et al. 2001; Hooper et al. 2004). Deriving the relationship between the phase delay and elevation is another simple and effective way to reduce tropospheric noise (Bekaert et al. 2015a; Murray et al. 2021). The second approach uses external datasets, such as meteorological data (Yu et al. 2018a), multispectral satellite imagery data, such as those from the MODerate resolution Imaging Spectroradiometer (MODIS) aboard the Terra and Aqua satellites (Li et al 2005, 2009), and the MEdium Resolution Imaging Spectrometer (MERIS) onboard ENVISAT (Li et al. 2006, 2009), or distributed Global Navigation Satellite System (GNSS) network data (Shamshiri et al. 2020). These two types of approaches can also be used simultaneously.

In the present study, we explored and compared the characteristics of different tropospheric delay correction methods using numerical weather models and evaluated their suitability in Japan. Most of Japan is in a temperate climate zone and exhibits notable seasonal changes. Temperature and humidity are typically high during summer for most of central and western Japan. Since ~ 70% of the Japanese landmass is mountainous, the troposphere above it experiences extensive spatiotemporal variations compared to other places in the world. For these reasons, different tropospheric delay correction methods tend to lead to significantly different outputs, highlighting the importance of choosing a suitable correction method (Bekaert et al. 2015b).

The refractivity models, the weather model dataset, and the delay calculation algorithm should be considered for this comparison. Here, refractivity models refer to mathematical relationships wherein delay is expressed as a function of the dry pressure, partial pressure of water vapor, and temperature of the atmosphere.

The refractivity model proposed by Bevis et al. (1994) (hereafter BV94) is used by the Radar INterferometry Calculation (RINC) software used by the Japanese research community (Ozawa et al. 2016), the model of Berrada-Baby et al. (1988) (hereafter BB88) has been adopted by the Generic Atmospheric Correction Online Service (GACOS) for InSAR (Yu et al. 2018b), and the model of Smith and Weintraub (1953) (hereafter SW53) is used by the open-source package Toolbox for Reducing Atmospheric InSAR Noise (TRAIN) (Bekaert et al. 2015b). There are other refractivity models, such as those proposed by Bevis et al. (1992) or Aparicio and Laroche (2011), but we focused on the models used by widely available software for InSAR tropospheric delay correction in the present study.

As for the algorithm, many studies and software packages, including RINC and TRAIN, calculate the delay along the radar line-of-sight (LOS) direction, whereas GACOS calculates the delay in the vertical direction using an iterative tropospheric decomposition (ITD) method (Yu et al. 2018a), which is later projected into the LOS direction by the users.

As for the dataset, the mesoscale model (MSM), which is published by the Japan Meteorological Agency (JMA), has relatively dense sampling (with horizontal grid spacing of 5 km and temporal resolution of 3 h), is available for the whole area in Japan, and is compatible with the RINC software. On the other hand, GACOS uses the HRES-ECMWF, a 10-day forecast product, which covers the worldwide area with spatial and temporal resolutions of 14 km and 6 h, respectively.

As explained by the diagram in Fig. 1, we made two comparisons, first on the differences in the performance of tropospheric noise correction obtained from the three refractivity models mentioned above (BV94, BB88, and SW53) ("Comparison of the three refractivity models"), and second on those obtained from RINC and GACOS ("Comparison of tropospheric correction of RINC and GACOS"). We made these comparisons on ionospheric-corrected interferograms.

Data and methods

Study area

We selected two areas on Honshu Island, Japan, as the study area (Fig. 2a). The first study area was in the Tohoku region, located in the northern part of the island; the relief in this area consists of plains and mountainous areas (Fig. 2b). Trending north to south, the Ou Mountains greatly influence airflow in the troposphere above it. The mitigation of tropospheric delay in this area is motivated by the fact that this tectonically active zone hosts large earthquakes and volcanoes, including the Mw 6.9 2008 Iwate-Miyagi Nairiku Earthquake (Ohta et al. 2008; Okada et al. 2010). The second study area was in the Kansai region of western Honshu (Fig. 2c); this region has a sharper contrast in topographic relief than the first study area. The region is traversed by major active faults, such as the Arima-Takatsuki, Ikoma, and Uemachi faults. This area also includes the location of the 2018 northern Osaka earthquake (Mw 5.6), a shallow crustal earthquake on the northeastern edge of the Osaka Plain (Kato and Ueda 2019). The tectonic deformation signals

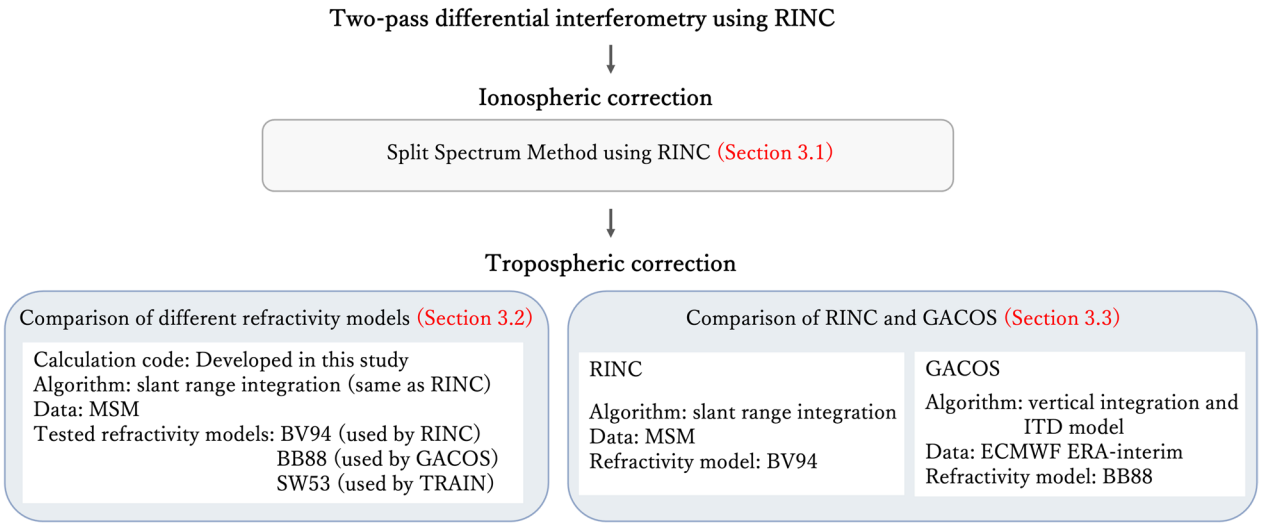

Fig. 1 Framework of this study to perform the comparison of different tropospheric correction methods. BV94, BB88, and SW53 refer to the refractivity models of Bevis (1994), Berrada-Baby et al. (1988), and Smith and Weintraub (1953), respectively

expected from the above-mentioned earthquakes and other tectonic processes are less than a few mm; hence, the present study neglected the ground deformation and assumed that the coherent phase changes in the interferograms were mainly due to tropospheric and ionospheric noise.

InSAR processing

To evaluate the performance of tropospheric delay correction in the study areas, we used SAR images from Advanced Land Observing Satellite-2 (ALOS-2)/Phased Array type L-band Synthetic Aperture Radar (PALSAR-2) in the StripMap (SM1) mode. Detailed information on the SAR observations is summarized in Table 1. For the Tohoku region, we used 10 images from 2014 to 2018 from Path 18, Frame 2830 (descending orbit), and 12 images from 2015 to 2019 from Path 124 and Frame 770 (ascending orbit); the incidence angles were 35.9° for both datasets. We used 12 images from 2015 to 2019 from Path 128 and Frame 680 (ascending) for the Kansai region, with an incidence angle of 38.2°.

An interferogram is calculated from a pair of SAR images by taking the difference between the phases of the first (primary) and second (secondary) acquisitions to measure the surface displacement that occurred between acquisitions in the LOS direction as well as atmospheric delay effects and other noise terms. We processed the interferograms for each study area using the RINC software (Ozawa et al. 2016) with range and azimuth look numbers of 8 and 10, resulting in a spatial resolution of approximately 20×20 m. A spectrum filter with a 32×32-pixel window size was applied to reduce decorrelation (Baran et al. 2003). We used ellipsoidal height data generated from a 10-m mesh digital elevation model, published by the Geospatial Information Authority of Japan (GSI), and the Earth Gravitational Model 96 (EGM96) geoid model (Lemoine et al. 1997) to remove topographic fringes and geocode the interferograms. The differential phase values were unwrapped using Statistical-Cost, Network-Flow Algorithm for Phase Unwrapping (SNAPHU) (Chen and Zebker 2000).

Tropospheric correction methods

Slant delay integration

The total tropospheric delay can be estimated by integrating the delay along the propagation path of the microwave in the slant LOS direction (Additional file 1: Fig. S1). The total tropospheric delay is calculated in the straight line from topography to the upper limit of the tropospheric layer. The geometric delay due to the bending effect was not considered in this study (Ozawa et al. 2019). The slant-delay integration method generally involves three processing steps. The first step is to resample meteorological data to a regular latitude-longitude-height grid. The next step is the interpolation of the data along the path, and the final step is the integration of refractivity from ground (r_1) to the upper limit of troposphere (r_2), using the following general equations (Hanssen 2001):

$$N = N_{\mathrm{dry}} + N_{\mathrm{wet}} = \left(k_1 \frac{P}{T}\right) + \left(k_2 \frac{e}{T} + k_3 \frac{e}{T^2}\right) \quad (1)$$

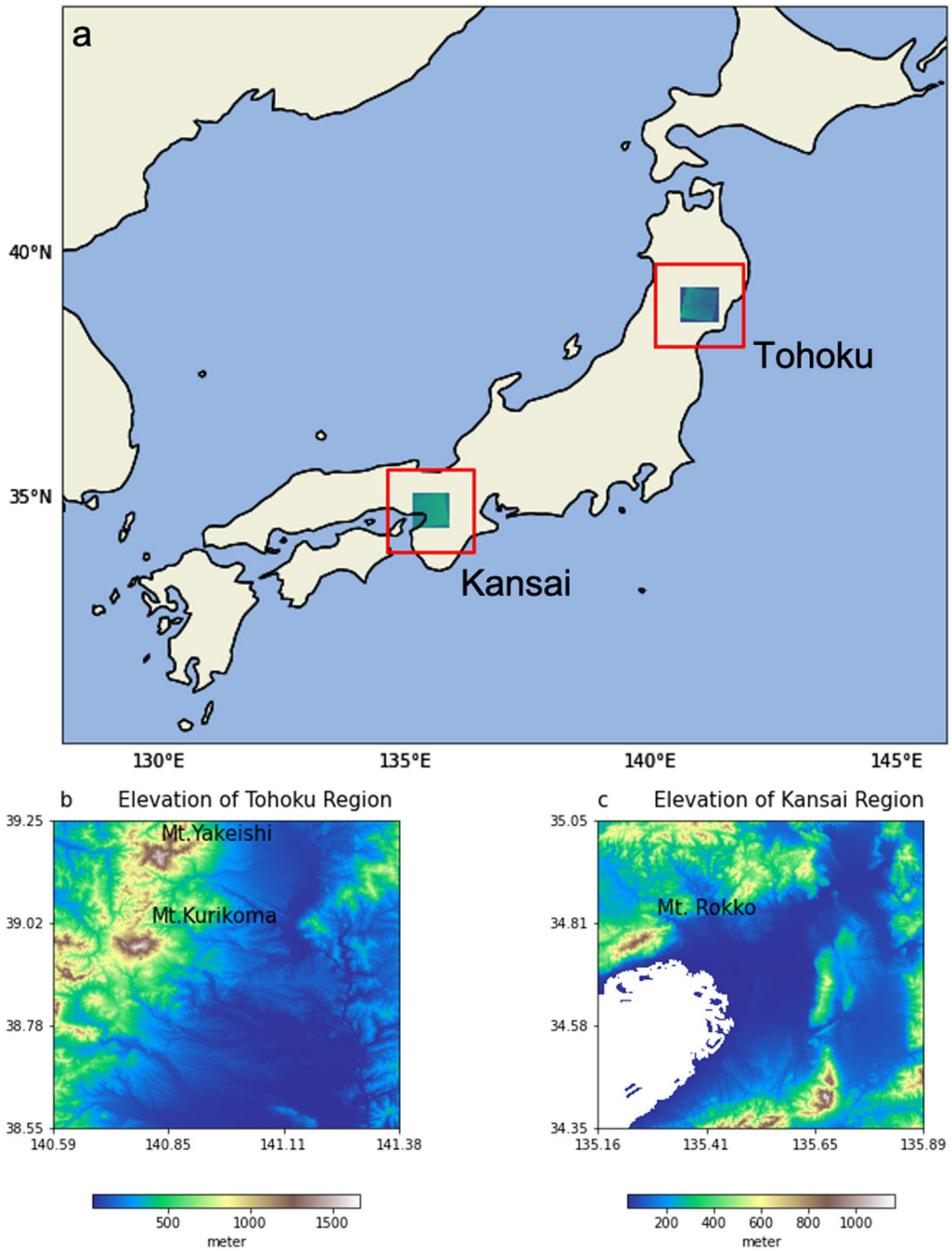

Fig. 2 **a** Map of Japan with two study areas shown with red rectangles. **a**, **c** Elevation maps for the Tohoku and Kansai regions

Table 1 SAR images information for the Tohoku and Kansai regions

Area	Sensor	Path-frame	Orbit/Inc. angle	Time coverage	Number of images
Tohoku	PALSAR-2	18–2830	Descending/32.8°	Aug 2014–Aug 2018	10
Tohoku	PALSAR-2	124–770	Ascending/35.9°	Jun 2015–Jan 2019	12
Kansai	PALSAR-2	128–680	Ascending/38.2°	Apr 2015–Jun 2019	12

$$\Delta L = 10^{-6} \int_{r_1}^{r_2} [Nds] = 10^{-6} \left[\int_{r_1}^{r_2} \left(k_1 \frac{P}{T} + k_2 \frac{e}{T} + k_3 \frac{e}{T^2} \right) ds \right] \quad (2)$$

where N is the refractivity index, ΔL is the total delay, $_P$ is the dry pressure of the atmosphere, T is the temperature, and e is the partial pressure of the water vapor. Different values of the constants k_1,k_2, and k_3 have been proposed in different refractivity models (Table 2).

In this study, we used the RINC software (Ozawa et al. 2016) to read and resample MSM data. We then computed the delay after linear interpolation of the data and applied Eqs. 1 and 2 with different constant values. The sets of constants k_1, k_2, and k_3 corresponding to the models of BV94 (used by RINC), BB88 (used by GACOS), and SW53 (used by TRAIN) were used to calculate the delay (Table 2) and the results are compared in "Comparison of the three refractivity models":

GACOS method

Yu et al. (2018a) proposed a method to incorporate delay data estimated using GNSS data into numerical weather model data. The authors provided a GACOS correction that delivers delay estimates computed by the method, although the website (http://www.gacos.net, last accessed on 9 September 2022) stated that only the numerical weather model is used. GACOS uses the HRES-ECMWF numerical weather model, which has a grid spacing of 0.125° with 137 vertical levels and temporal sampling of 6 h. To better estimate the stratified and turbulent delay components, GACOS uses the iterative tropospheric decomposition (ITD) method (Yu et al. 2018a). For the refractivity model, GACOS uses the equation proposed by Berrada-Baby et al. (1988), neglecting the bending effect, which is as follows:

$$\mathrm{ZTD} = 10^{-6} \int_{r_1}^{r_2'} [Ndz] = 10^{-6} \left[\frac{k_1 R_1}{gm} P_{(Z0)} + \int_{r_1}^{r_2'} \left(k_2' \frac{e}{T} + k_3 \frac{e}{T^2} \right) dz \right] \quad (3)$$

where the integral is calculated vertically between the ground surface, r_1 and upper boundary of the troposphere (or the height above the ground), r_2'. $P_{(Z0)}$ is the surface pressure at the topography, R_1 is the ideal gas constant, gm is the gravitational acceleration averaged over the troposphere, and k_1 and k_3 are the same constants as defined in Eq. 2. The constant k_2' is related to k_2 with $k_2' = k_2 - 0.622k_1$ (Berrada-Baby et al. 1988). The ZTD was projected to the LOS direction, and the bending effect was neglected.

Results

Interferograms with ionospheric correction

L-band interferograms are often severely affected by ionospheric disturbances. The ionospheric noise in the original interferograms is depicted as irregular fringes (Additional file 1: Figs. S2a, S2b, and S3). The application of the split-spectrum method (Gomba et al. 2015) effectively mitigated the ionospheric noise in the two study areas, shown as flattened fringe patterns in the interferograms (Fig. 3, Additional file 1: Fig. S4, and S5).

We calculated the standard deviation of each of the 51 interferograms, before and after the corrections, to assess the performance of the ionospheric correction method (Additional file 1: Tables S1, S2, and S3). If the standard deviation decreased after the correction, it means that the correction was effective. After applying the ionospheric corrections, the mean standard deviation of the interferograms decreased from 2.33 to 1.19 cm for the Kansai ascending dataset, 2.97 to 1.71 cm for the Tohoku ascending dataset, and 3.42 to 0.87 cm for the Tohoku descending dataset. We also assessed the spatial correlation of noise before and after the correction using a semi-variogram, a regression curve of semi-variogram at different distances (Liebhold et al. 1991). The semi-variogram is defined as the following equation:

$$\gamma(h) = \frac{1}{2N(h)} \sum_{i=1}^{N(h)} \left[Z_{x_i} - Z_{x_i+h} \right]^2 \quad (4)$$

where Z_{x_i} is the observation value at the i-th location x_i, h is the distance, and $N(h)$ is the number of point pairs at that distance. Semi-variograms showed that the long-wavelength variations were significantly reduced by ionospheric correction (Additional file 1: Fig. S6). For

Table 2 List of the coefficients for each refractivity model

Refractivity model	k_1 (K/hPa)	k_2 (K/hPa)	k_2' (K/hPa)	k_3 (K^2/hPa)	R_1 (JK/kg)
SW53 (Smith and Weintraub 1953)	77.6	23.3		3.75×10^5	
BV94 (Bevis 1994)	77.6	70.4		3.739×10^5	
BB88 (Berrada-Baby et al. 1988)	77.6		23.3	3.75×10^5	287.05

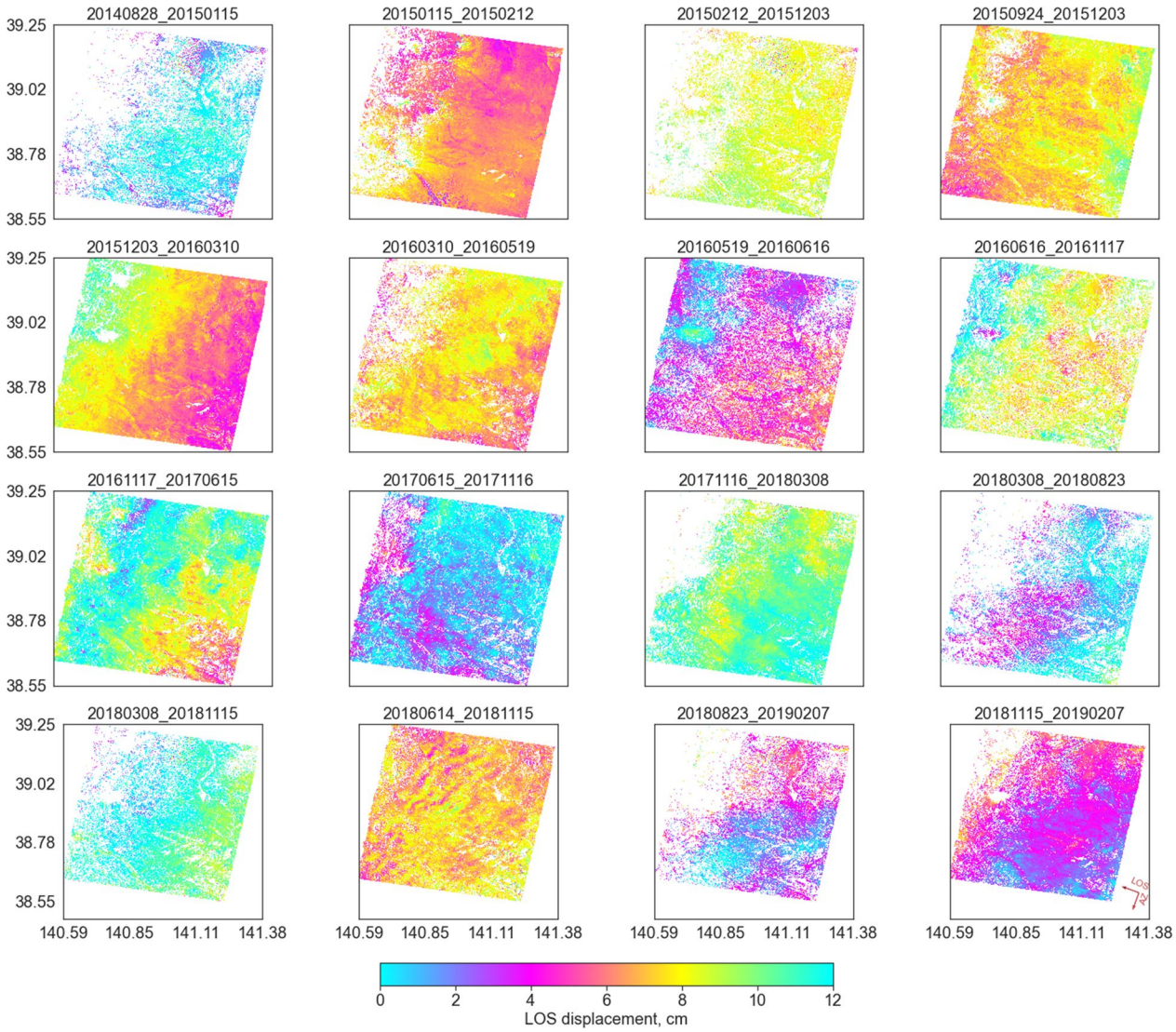

Fig. 3 Examples of ionosphere-corrected descending interferograms obtained using the split-spectrum method for the Tohoku region. The acquisition dates are shown above each interferogram. The incoherent pixels with a coherence threshold < 0.12 were masked in this figure

the remainder of this paper, we have used ionospheric-corrected interferograms to evaluate tropospheric delay corrections.

Comparison of the three refractivity models

Tropospheric delays were predicted using the Bevis (1994) (BV94), Smith and Weintraub (1953) (SW53), and Berrada-Baby et al. (1988) (BB88) models. The difference between BV94 and SW53 is the value of the constant, and the difference between BV94 and BB88 is in the hydrostatic component calculations.

We used an identical MSM dataset to compare tropospheric correction terms estimated from the three refractivity models. In this experiment, we adopted the slant range integration method ("Slant delay integration"). Since the RINC software can only be used with the BV94 model, we programmed a code whose algorithm (except for the refractivity model) is the same as RINC and used it to make the calculations assuming the three refractivity models. Our codes were verified to produce results identical to the RINC outputs, with a difference of less than 0.01 mm.

Examples of the delay calculation results of the Tohoku and Kansai regions are shown in Figs. 4 and 5 and Additional file 1: Figs. S7 and S8, respectively. In these figures, a darker color indicates a smaller delay in higher-altitude areas and thus reflects a shorter propagating path. In some cases, the estimated tropospheric delay in a single

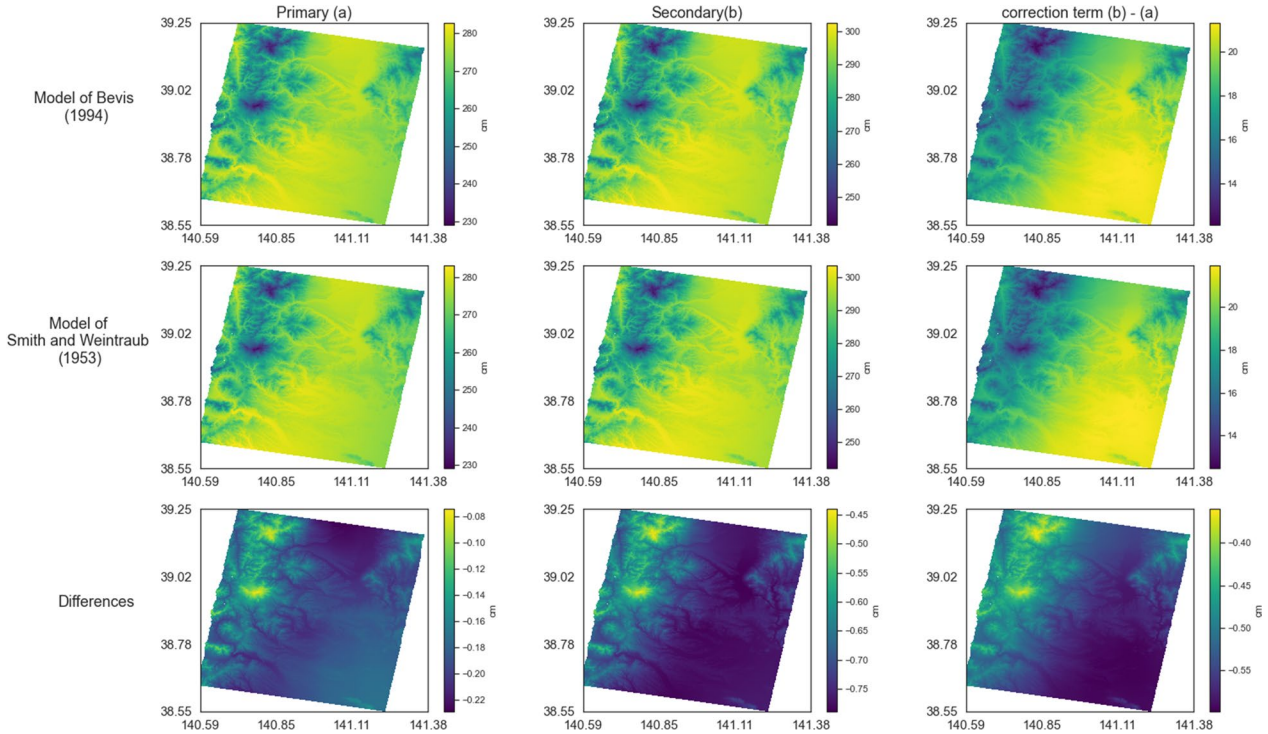

Fig. 4 Examples of tropospheric delay predicted in the Tohoku region obtained using the slant-delay integration method from the refractivity models of Bevis (1994) (top), Smith and Weintraub (1953) (middle), and the differences between the two models (bottom). **a** Delay predicted for the primary image obtained on 19 May 2016. **b** Delay predicted for the secondary image obtained on 16 June 2016. **c** Correction term calculated by the difference in the delay on the two acquisition dates

epoch could exceed 3 m, indicating a significant tropospheric effect. The correction term for InSAR tropospheric delay was calculated by subtracting the delay of the primary acquisition from that of the secondary acquisition. Results indicated that the calculated correction terms in both study areas were up to 24 cm for all refractivity models; differences in the correction terms ranged up to a few centimeters. The variation in the differences within a scene, which is directly related to the difference in the effectiveness of the correction, was even smaller (0.55–1.55 cm) in the example shown in Fig. 6.

Differences were statistically evaluated by calculating the mean standard deviation over the entire interferogram of all the tested interferograms. The standard deviation among the three refractivity models shows minor differences (Additional file 1: Figs. S9 and S10), but the BV94 model produced the lowest mean standard deviation (Table 3). In the Kansai region, tropospheric corrections using the models of BV94, BB88, and SW53 reduced the standard deviation from 1.19 to 1.09, 1.09, and 1.09 cm, respectively. This result indicated that tropospheric correction using the aforementioned method is effective, and the difference in the mean standard deviation after corrections was less than 0.01 cm, which is consistent with the findings of a study by Aparicio and Laroche (2011), who found that the differences between their refractivity model and other models, including BV94 and SW53, were within 0.1% RMS (root mean square). Similarly, tropospheric noise correction using the three models all reduced the mean standard deviation from 0.87 to 0.78 cm in the Tohoku region.

Comparison of tropospheric correction of RINC and GACOS

We compared the tropospheric correction products derived from the RINC (Ozawa et al. 2016) and GACOS (Yu et al. 2018a). The RINC calculates delay along the slant direction connecting the ground and satellite using the equations provided by the refractivity model BV94 and the MSM data of JMA. The GACOS adopts the zenith integration approach and uses the HRES-ECMWF and the refractivity model of BB88.

Figure 7 shows the absolute delay distributions obtained using the RINC and GACOS methods. In most cases, RINC predicted a greater delay and less detailed topographical variation than GACOS, with differences of up to 4 cm (Fig. 7).

The RINC and GACOS correction products were compared by calculating the tropospheric noise term

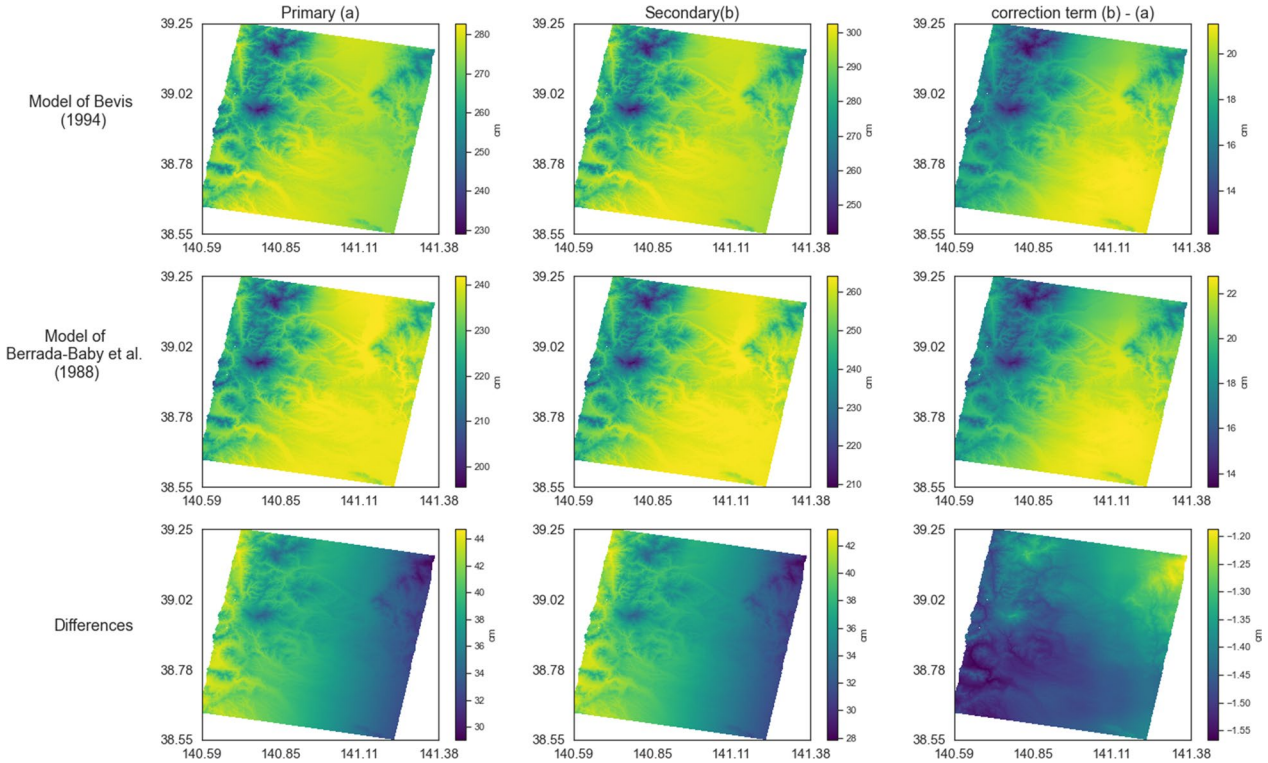

Fig. 5 Examples of tropospheric delay predicted in the Tohoku region obtained using the slant-delay integration method from the refractivity models of Bevis (1994) (top) and Berrada-Baby et al. (1988) (middle) and the difference between the two models (bottom). **a** Delay predicted for the primary image. **b** Delay predicted for the secondary image. **c** Correction term calculated by subtracting the delay on the two acquisition dates. The acquisition dates are identical to those shown in Fig. 4

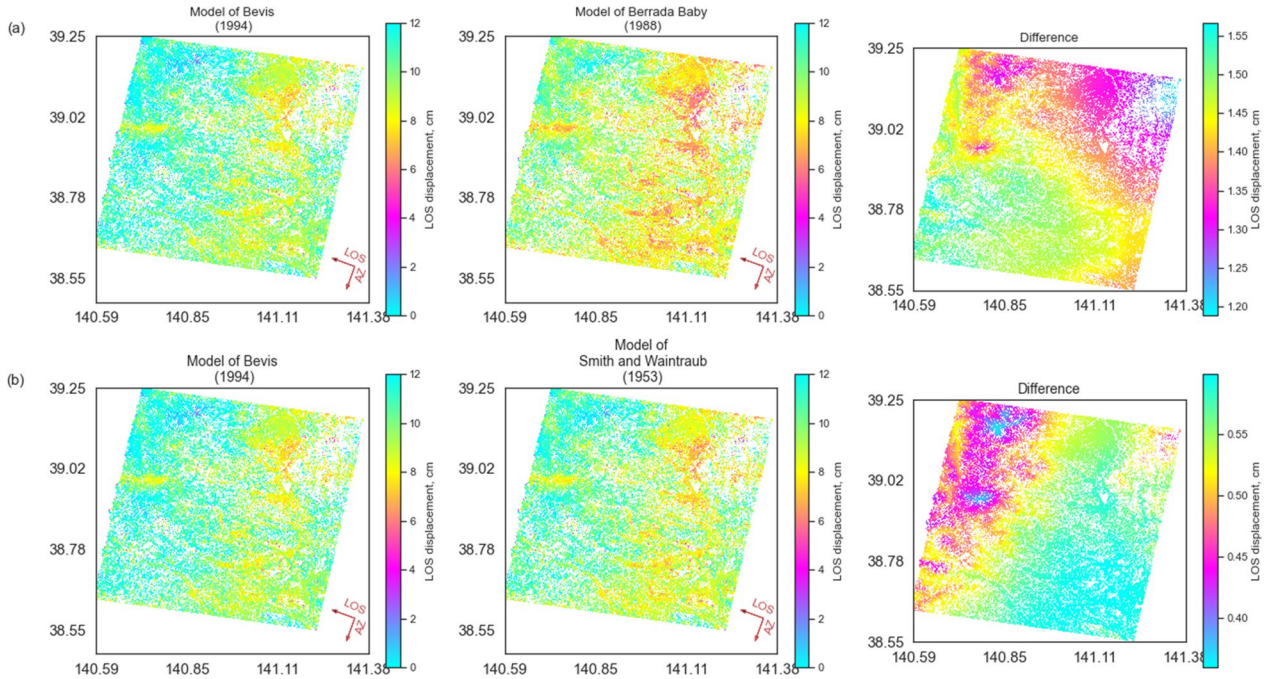

Fig. 6 **a** Examples of corrected interferograms obtained using the models of Bevis (1994) and Smith and Weintraub (1953) in the Tohoku region. **b** Examples of corrected interferograms obtained using the models of Bevis (1994) and Berrada-Baby et al. (1988) in the Tohoku region. The acquisition dates are identical to those shown in Fig. 4

Table 3 Mean standard deviation of interferograms, before and after correction

Regional details	Reference (cm)	BV94 (cm)	BB88 (cm)	SW53 (cm)
Tohoku/Descending	0.87	0.78	0.78	0.78
Tohoku/Ascending	1.71	1.33	1.33	1.34
Kansai/Ascending	1.19	1.09	1.09	1.09

(i.e., the difference between the delays of the first and second acquisitions) and subtracting it from the ionosphere-corrected interferogram, as shown in Fig. 8. The results showed that both methods reduced the tropospheric delays in 68% of the interferograms in both areas; however, a significant amount of tropospheric noise was still present in the corrected interferograms. We statistically assessed the performances of the RINC and GACOS methods. In most interferograms, correction reduced the standard deviation of the LOS displacements, but this was not always the case (Fig. 9). Tropospheric correction was effective in mountainous areas (i.e., stratified components) but not in flat areas (i.e., turbulent components) ("Evaluation of tropospheric delay in mountainous and flat areas"). The mean standard deviation of all interferograms in the Tohoku region decreased from 0.87 to 0.78 cm for

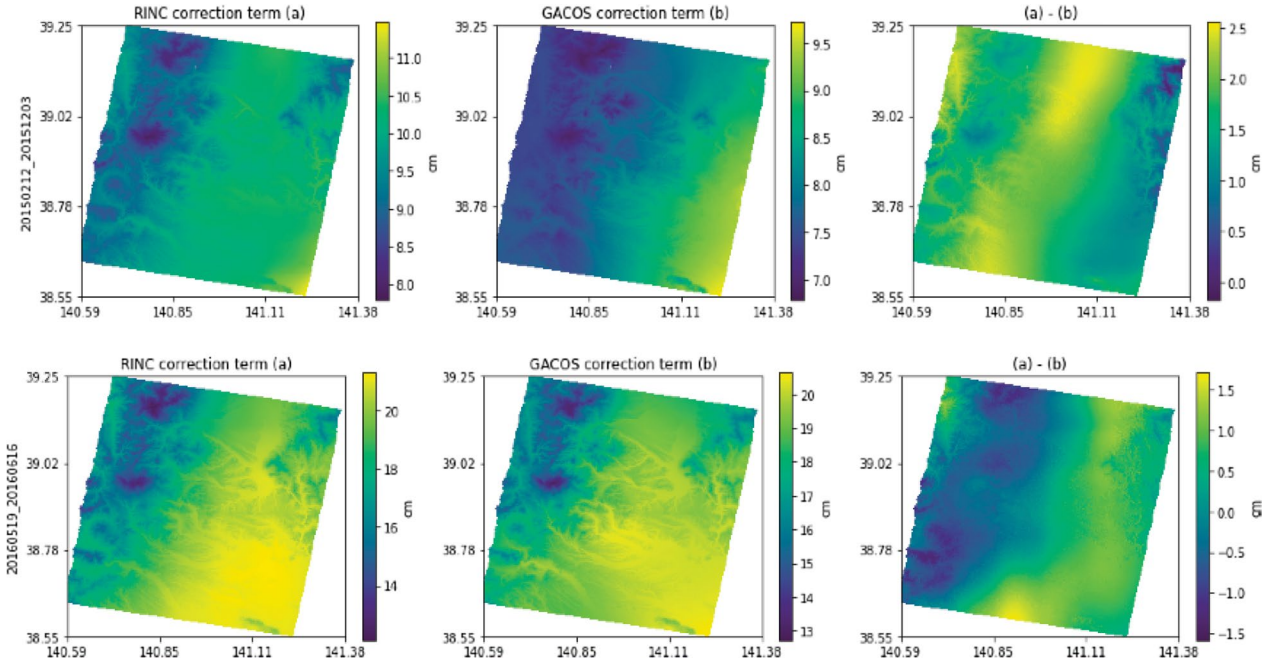

Fig. 7 Correction terms from RINC and GACOS and the differences between the two methods were calculated for two interferograms in the Tohoku region. The acquisition dates are shown on the left side of the figures

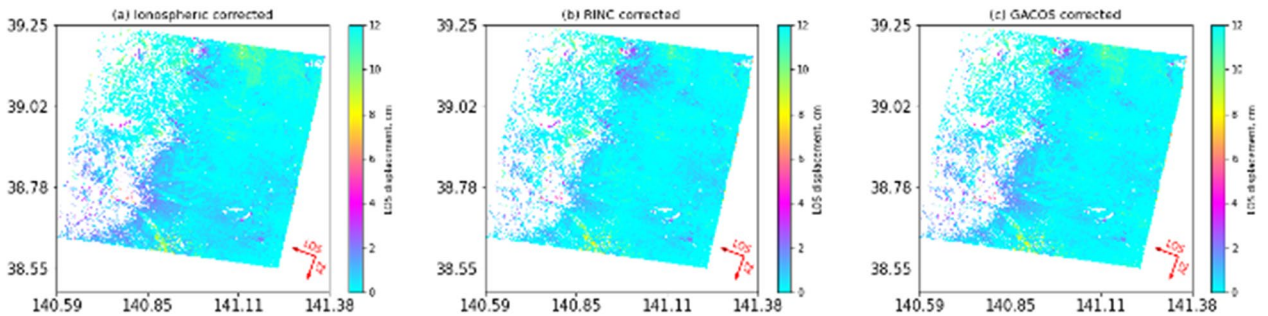

Fig. 8 **a** Example of an ionosphere-corrected interferogram in the Tohoku region. **b** Interferogram with GACOS correction applied on **a**. **c** Interferogram with RINC correction applied on **a**. The decorrelated parts shown in these interferograms were excluded from the statistical comparison. The primary image was obtained on January 15, 2015. The secondary image was acquired on February 12, 2015

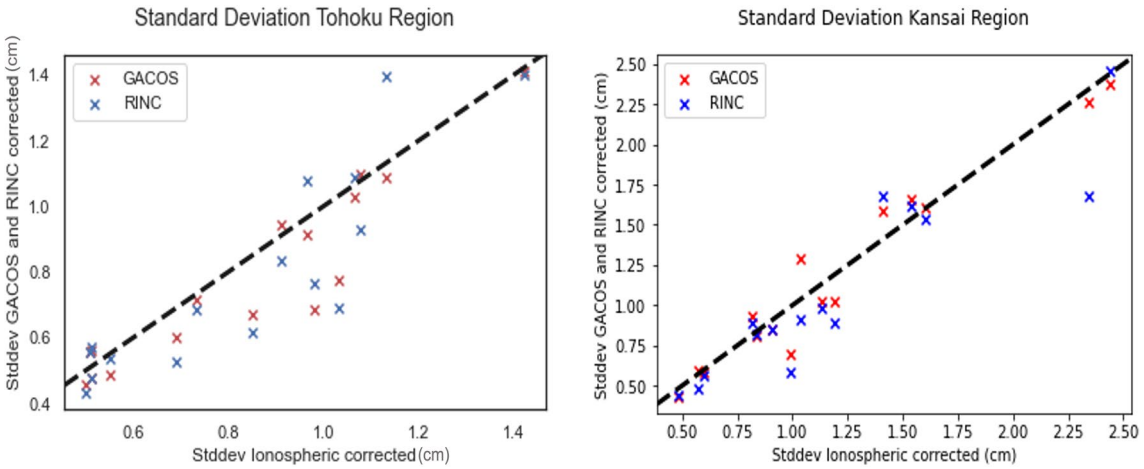

Fig. 9 Standard deviations after tropospheric corrections using RINC and GACOS in the two study areas plotted against the standard deviations before the tropospheric corrections (reference). Marks below the broken line (standard deviations before and after correction are equal) indicate that the corrections worked as expected

both correction methods. The assessment of the Kansai region data led to a slightly different result; the mean standard deviation decreased from 1.19 to 1.09 and 1.10 cm after applying the RINC and GACOS corrections, respectively, indicating a slightly better performance from the RINC correction.

Discussion

Evaluation of tropospheric delay corrections in the Tohoku and Kansai regions

The Kansai and Tohoku regions analyzed in the present study had different conditions depending on topographic relief (Fig. 2b, c), atmospheric conditions during the acquisition time, and coherence of the interferogram data. Therefore, the effectiveness of these corrections was expected to vary. The mean standard deviation of signals before tropospheric correction in ascending interferograms in the Kansai region was smaller than that in the Tohoku region, as shown in Table 3.

The effectiveness of the tropospheric delay correction was at a similar level for the two regions if the same correction software (RINC or GACOS) was used. With respect to different topographical features, it is possible that the effectiveness of the correction may be different in mountainous and flat areas, as discussed further in "Evaluation of tropospheric delay in mountainous and flat areas".

Evaluation of tropospheric delay in mountainous and flat areas

Mountainous areas contain both stratified and turbulent components of tropospheric delay, while flat areas contain only a turbulent component. This section separately focuses on the flat and mountainous areas and compares them (Additional file 1: Fig. S11). Similar to what has been found in previous studies, our results showed higher standard deviations in mountainous areas (Table 4) (Yu et al. 2018b). In the Kansai region, tropospheric correction improved the interferogram by reducing the mean standard deviation from 0.98 to 0.89 cm in mountainous areas; the mean standard deviation decreased from 0.29 to 0.25 cm in the plains. In the Tohoku region, the mean standard deviation

Table 4 Mean standard deviation of mountainous and flat areas in interferograms

Regional details	Type of terrain	Reference(cm)	BV94(cm)	BB88(cm)	SW53(cm)
Tohoku/Descending	Mountain	1.71	1.53	1.53	1.53
	Flat	1.14	0.92	0.92	0.92
Tohoku/Ascending	Mountain	1.37	1.30	1.29	1.29
	Flat	0.49	0.47	0.47	0.47
Kansai/Ascending	Mountain	0.98	0.89	0.90	0.90
	Flat	0.29	0.20	0.25	0.25

decreased from 1.37 to 1.30 cm for ascending interferograms and 1.71 to 1.53 cm for descending interferograms by tropospheric correction in the mountainous areas. In the flat areas in Tohoku, the mean standard deviation decreased from 0.49 and 1.14 cm to 0.47 and 0.92 cm for ascending and descending interferograms, respectively. Based on these results, it can be concluded that: (1) tropospheric delay is more substantial in mountainous areas, (2) tropospheric correction is more effective in mountainous areas, and (3) correction is imperfect yet effective in the flat areas.

Comparison of atmospheric delay on ascending and descending interferograms

Atmospheric conditions over the same areas vary significantly with time. This study compared atmospheric delays in the ascending and descending interferograms in the Tohoku region. Ascending and descending interferograms were acquired at 11:42 and 23:58 local time, respectively. Table 3 shows the values of the mean standard deviation before correction, i.e., 1.71 cm and 0.87 cm for ascending and descending interferograms, respectively, indicating greater noise in the ascending interferograms. The tropospheric delay correction reduced the mean standard deviation of both the ascending and descending interferograms (Table 3) but still indicated the presence of greater noise in the ascending interferograms. In the ascending interferograms, after corrections (Additional file 1: Fig. S4), long-wavelength noise and altitude did not have a direct correlation. We infer that this is mainly due to greater difficulties for the numerical weather model in reproducing turbulence around noon local time.

Comparison with other studies

Stephens et al. (2020) found that the applicability of the correction method is highly case-dependent, showing there is no global weather model that can accurately capture the tropospheric delay. In our study, the tropospheric correction reduced the standard deviation up to 33% in 68% of interferograms in the Tohoku region and up to 41% in 66% of interferograms in the Kansai region (Additional file 1: Tables S1, S2, S3). These results showed that the corrections using RINC and the MSM weather model are as effective as the case studies over the Usu volcano in Japan that successfully reduced standard deviation in 45% of the interferograms using the GACOS product (Wang and Aoki 2019). The reduction in the standard deviation varied from approximately 35% to 45% over the Agung Volcano in Bali, Indonesia, which was obtained using GACOS with HRES-ECMWF data (Albino et al. 2019) and is comparable to our results. Our results using GACOS, reducing the standard deviation up to 40% in 73% of interferograms, indicate better performance than other studies that indicated insignificant improvement using GACOS (Guo et al. 2019). This suggests that the approach of using numerical weather models is effective over Japan.

Conclusions

This study confirmed that ionospheric delays heavily impact ALOS-2 L-band interferograms in Japan and that the mitigation of ionospheric delays works effectively using the split-spectrum method.

Tropospheric correction using three models—Bevis (1994), Berrada-Baby et al. (1988), and Smith and Weintraub (1953)—was applied to 51 interferograms in 2 different regions. Performance assessment of the three refractivity models showed insignificant differences in mean standard deviation and semi-variance. We concluded that all three refractivity models can be used to calculate tropospheric delay.

Tropospheric correction terms obtained using the RINC and GACOS methods showed differences up to 4 cm, and the mean standard deviation after RINC correction in the two studied areas was slightly smaller than the GACOS result; this indicates a slightly better performance of RINC correction. This can be either due to the use of the MSM mesoscale model, which has higher temporal and spatial resolutions or to the difference in the calculation scheme.

Abbreviations

ALOS-2	Advanced Land Observing Satellite-2
ECMWF	European Centre for Medium-Range Weather Forecasts
EGM96	Earth Gravitational Model 96
GACOS	Generic Atmospheric Correction Online Service
GSI	Geospatial Information Authority of Japan
GNSS	Global navigation satellite system
HRES	High-resolution forecast
ITD	Iterative tropospheric decomposition
JMA	Japan Meteorological Agency
LOS	Line of sight
InSAR	Interferometric synthetic aperture radar
MERIS	MEdium resolution imaging spectrometer
MODIS	MODerate resolution imaging Spectroradiometer
MSM	Mesoscale model
RINC	Radar INterferometry calculation tools
RMS	Root mean square
SAR	Synthetic aperture radar
SNAPHU	Statistical-cost, Network-flow Algorithm for Phase Unwrapping
TRAIN	Toolbox for reducing atmospheric InSAR noise
PALSAR	Phased Array Type L-band Synthetic Aperture Radar
PIXEL	PALSAR Interferometry Consortium to Study our Evolving Land surface
ZTD	Zenith total delay

Supplementary Information

The online version contains supplementary material available at https://doi.org/10.1186/s40623-023-01773-z.

Additional file 1. Figure S1. Schematic for the slant delay integration method. The black arrow represents the microwave propagation direction, shades of grey represent the hydrostatic equilibrium of the tropospheric layer, the dashed line represents the center lines for each layer, and the green line illustrates the topography. **Figure S2.** (a) Ascending and (b) descending interferograms in the Tohoku region before ionospheric and tropospheric corrections. The acquisition dates are indicated above the figures. **Figure S3.** Ascending interferograms in the Kansai region before ionospheric and tropospheric corrections. The acquisition dates are indicated above the figures. **Figure S4.** The ionospheric-corrected ascending interferograms obtained using the split-spectrum method for the Tohoku region. Ionospheric-corrected descending interferograms using the same method are shown in Figure 3. **Figure S5.** Examples of ionospheric-corrected interferograms in the Kansai region. **Figure S6.** The semi-variance of the original and ionospheric-corrected interferogram in the Kansai Region. **Figure S7.** Examples of tropospheric delay predicted in the Kansai region were obtained using the slant-delay integration method proposed by Bevis (1994) (top row), Smith and Weintraub (1953) (middle), and the differences between the two models (bottom). (a) Delay predicted for the primary image obtained on 19 April 2018. (b) Delay predicted for the secondary image obtained on 18 June 2018. (c) Correction term calculated by the difference in the two acquisition dates. **Figure S8.** Examples of tropospheric delay predicted in the Kansai region were obtained using the slant-delay integration method, proposed by Bevis (1994) (top row), Berrada-Baby et al. (1988) (middle), and the differences between the two models (bottom). (a) Delay predicted for the primary image obtained on 19 April 2018. (b) Delay predicted for the secondary image 18 June 2018. (c) Correction term calculated by the difference in the two acquisition dates. **Figure S9.** Mean standard deviation of three refractivity models in the two study areas. The X and Y axes show the standard deviation for the ionospheric-corrected interferogram (reference) and the three refractivity models, respectively. The broken line represents the value of X equal to Y. **Figure S10.** Mean standard deviation of RINC and GACOS in the two study areas. **Figure S11.** Areas in which the standard deviations were calculated (shown as rectangles) for the (a) Kansai region and (b) Tohoku region. Red represents mountainous areas, and orange indicates flat areas. **Table S1.** The standard deviation of the methods, before and after correction in the Tohoku region (descending). **Table S2.** The standard deviation of the methods, before and after correction in the Tohoku region (ascending). **Table S3.** The standard deviation of the methods, before and after correction in the Kansai region.

Acknowledgements
We partly used the PALSAR-2 SLC data shared among PALSAR Interferometry Consortium to Study our Evolving Land Surface (PIXEL) and provided by JAXA under a cooperative research contract with PIXEL and partly used the PALSAR-2 SLC data provided through a research contract with JAXA. This work was supported in part by the JST SPRING with grant number JPMJSP2114, the WISE Program for Sustainability in the Dynamic Earth, and by ERI JURP 2021-B-03 at the Earthquake Research Institute of the University of Tokyo. We used RINC software developed by Dr. Ozawa of the National Research Institute for Earth Science and Disaster Resilience of Japan. The MSM weather model data were obtained from the JMA and were provided by RISH, Kyoto University. We used the GACOS method developed by the University of New Castle. The HRES-ECMWF is recognized for its high-resolution tropospheric products.

Author contributions
Sardila Nurulhikmah Sailellah conducted InSAR processing and data analysis, prepared figures, and wrote the manuscript. Yo Fukushima supervised the InSAR data analysis and co-wrote the manuscript. Both the authors discussed and revised the manuscript accordingly.

Funding
This study was supported by JST SPRING, with grant number JPMJSP2114.

Availability of data and materials
ALOS-2 data are obtained from JAXA and provided by the PIXEL community.

Declarations

Ethics approval and consent to participate
Not applicable.

Consent for publication
Not applicable.

Competing interests
The authors declare that they have no competing interests.

Author details
[1]Graduate School of Science, Tohoku University, Aramaki Aza-Aoba 468-1, Aoba-Ku, Sendai 980-0845, Japan. [2]International Research Institute of Disaster Science, Tohoku University, Aramaki Aza-Aoba 468-1, Aoba-Ku, Sendai 980-0845, Japan.

Received: 13 May 2022 Accepted: 18 January 2023
Published online: 02 February 2023

References

Albino F, Biggs J, Syahbana DK (2019) Dyke intrusion between neighbouring arc volcanoes responsible for 2017 pre-eruptive seismic swarm at Agung. Nat Commun 10:748. https://doi.org/10.1038/s41467-019-08564-9
Aparicio JM, Laroche S (2011) An evaluation of the expression of the atmospheric refractivity for GPS signals. J Geophys Res. https://doi.org/10.1029/2010jd015214
Baran I, Stewart MP, Kampes BM, Perski Z, Lilly P (2003) A modification to the Goldstein radar interferogram filter. IEEE Trans Geosci Remote Sens 41:2114–2118. https://doi.org/10.1109/TGRS.2003.817212
Bekaert DPS, Hooper A, Wright TJ (2015a) A spatially variable power law tropospheric correction technique for InSAR data. J Geophys Res 120:1345–1356. https://doi.org/10.1002/2014jb011558
Bekaert DPS, Walters RJ, Wright TJ, Hooper AJ, Parker DJ (2015b) Statistical comparison of InSAR tropospheric correction techniques. Remote Sens Environ 170:40–47. https://doi.org/10.1016/j.rse.2015.08.035
Bekaert DPS, Segall P, Wright TJ, Hooper AJ (2016) A network inversion filter combining GNSS and InSAR for tectonic slip modeling. J Geophys Res 121:2069–2086. https://doi.org/10.1002/2015jb012638
Bekaert DPS, Hamlington BD, Buzzanga B, Jones CE (2017) Spaceborne synthetic aperture radar survey of subsidence in Hampton Roads, Virginia (USA). Sci Rep 7:14752. https://doi.org/10.1038/s41598-017-15309-5
Berrada-Baby H, Golé P, Lavergnat J (1988) A model for the tropospheric excess path length of radio waves from surface meteorological measurements. Radio Sci 23:1023–1038. https://doi.org/10.1029/rs023i006p01023
Bevis M, Businger S, Herring TA, Anthes RA, Rocken C (1992) GPS meteorology: Remote sensing of atmospheric water vapor using the global positioning system. J Geophys Res 97:15787–15801. https://doi.org/10.1029/92jd01517
Bevis M, Businger S, Chiswell S, Hering TA, Anthes RA, Rocken C, Ware RH (1994) GPS Meteorology: mapping zenith wet delays onto precipitable water. J Appl Meteorol 33:379–386
Bürgmann R, Rosen PA, Fielding EJ (2000) Synthetic aperture radar interferometry to measure earth's surface topography and its deformation. Annu Rev Earth Planet Sci 28:169–209. https://doi.org/10.1146/annurev.earth.28.1.169
Campbell MD, David Campbell M, Wise HM (2018) Growth faulting and subsidence in the Houston, Texas Area: guide to the origins, relationships,

hazards, potential impacts and methods of investigation: an update. J Geol Geosci. 2:001–053. https://doi.org/10.13140/RG.2.1.4396.5604
Chen CW, Zebker HA (2000) Network approaches to two-dimensional phase unwrapping: intractability and two new algorithms. J Opt Soc Am A Opt Image Sci vis 17:401–414. https://doi.org/10.1364/josaa.17.000401
Colesanti C, Wasowski J (2006) Investigating landslides with space-borne Synthetic Aperture Radar (SAR) interferometry. Eng Geol 88:173–199. https://doi.org/10.1016/j.enggeo.2006.09.013
Ferretti A, Prati C, Rocca F (2001) Permanent scatterers in SAR interferometry. IEEE Trans Geosci Remote Sens 39:8–20. https://doi.org/10.1109/36.898661
Fukushima Y, Ishimura D (2020) Characteristics of secondary-ruptured faults in the Aso Caldera triggered by the 2016 Mw 7.0 Kumamoto earthquake. Earth Planets Space. https://doi.org/10.1186/s40623-020-01306-y
Ghayournajarkar N, Fukushima Y (2020) Determination of the dipping direction of a blind reverse fault from InSAR: case study on the 2017 Sefid Sang earthquake, Northeastern Iran. Earth Planets Space 72:64. https://doi.org/10.1186/s40623-020-01190-6
Gomba G, Parizzi A, De Zan F, Eineder M, Bamler R (2015) Toward operational compensation of ionospheric effect in SAR interferograms: the split-spectrum method. IEEE Trans Geosci Remote Sens 54:1446–1461. https://doi.org/10.1109/TGRS.2015.2481079
Gong W, Meyer F, Webley P, Lu Z (2011) Methods of InSAR atmosphere correction for volcano activity monitoring. Proceeding of the 2011 IEEE Geoscience and Remote Sensing Symposium 1654–1657. https://doi.org/10.1109/IGARSS.2011.6049550
Guo Q, Xu C, Wen Y, Liu Y, Xu G (2019) The 2017 noneruptive unrest at the caldera of Cerro Azul volcano (Galápagos Islands) revealed by InSAR observations and geodetic modelling. Remote Sensing 11:1992. https://doi.org/10.3390/rs11171992
Hamiel Y, Fialko Y (2007) Structure and mechanical properties of faults in the North Anatolian Fault system from InSAR observations of coseismic deformation due to the 1999 Izmit (Turkey) earthquake. J Geophys Res. https://doi.org/10.1029/2006jb004777
Hanssen RF (2001) Radar Interferometry: Data Interpretation and Error Analysis. Springer Science & Business Media, Berlin
Hooper A, Zebker H, Segall P, Kampes B (2004) A new method for measuring deformation on volcanoes and other natural terrains using InSAR persistent scatterers: a new persistent scatterers method. Geophys Res Lett 31:993. https://doi.org/10.1029/2004GL021737
Hooper A, Segall P, Zebker H (2007) Persistent scatterer interferometric synthetic aperture radar for crustal deformation analysis, with application to Volcán Alcedo. Galápagos J Geophys Res 112:993. https://doi.org/10.1029/2006JB004763
Jolivet R, Agram PS, Lin NY, Simons M, Doin M-P, Peltzer G, Li Z (2014) Improving InSAR geodesy using Global Atmospheric Models. J Geophys Res [solid Earth] 119:2324–2341. https://doi.org/10.1002/2013jb010588
Kato A, Ueda T (2019) Source fault model of the 2018 M w 5.6 northern Osaka earthquake, Japan, inferred from the aftershock sequence. Earth Planets Space 71:1–9. https://doi.org/10.1186/s40623-019-0995-9
Lanari R, Mora O, Manunta M, Mallorqui JJ, Berardino P, Sansosti E (2004) A small-baseline approach for investigating deformations on full-resolution differential SAR interferograms. IEEE Trans Geosci Remote Sens 42:1377–1386. https://doi.org/10.1109/TGRS.2004.828196
Lemoine FG, Smith DE, Kunz L, Smith R, Pavlis EC, Pavlis NK, Klosko SM, Chinn DS, Torrence MH, Williamson RG, Cox CM (1997) The Development of the NASA GSFC and NIMA Joint Geopotential Model. In: Gravity, Geoid and Marine Geodesy. Springer, Berlin. 461–469
Li Z, Fielding EJ, Cross P, Preusker R (2009) Advanced InSAR atmospheric correction: MERIS/MODIS combination and stacked water vapour models. Int J Remote Sens 30:3343–3363. https://doi.org/10.1080/01431160802562172
Li Z, Muller J-P, Cross P, Fielding EJ (2005) Interferometric synthetic aperture radar (InSAR) atmospheric correction: GPS, moderate resolution imaging spectroradiometer (MODIS), and InSAR integration. J Geophys Res. https://doi.org/10.1029/2004jb003446
Li Z, Fielding EJ, Cross P, Muller J-P (2006) Interferometric synthetic aperture radar atmospheric correction: medium resolution imaging spectrometer and advanced synthetic aperture radar integration. Geophys Res Lett. https://doi.org/10.1029/2005gl025299
Liebhold AM, Zhang X, Hohn ME, Elkinton JS, Ticehurst M, Benzon GL, Campbell RW (1991) Geostatistical analysis of gypsy moth (Lepidoptera: Lymantriidae) egg mass populations. Environ Entomol 20:1407–1417. https://doi.org/10.1093/ee/20.5.1407
Massonnet D, Rossi M, Carmona C, Adragna F, Peltzer G, Feigl K, Rabaute T (1993) The displacement field of the Landers earthquake mapped by radar interferometry. Nature 364:138–142. https://doi.org/10.1038/364138a0
Massonnet D, Feigl KL (1998) Radar interferometry and its application to changes in the Earth's surface. Rev Geophys. https://doi.org/10.1029/97RG03139
Meyer F, Bamler R, Jakowski N, Fritz T (2006) The potential of low-frequency SAR systems for mapping ionospheric TEC distributions. IEEE Geosci Remote Sens Lett 3:560–564. https://doi.org/10.1109/LGRS.2006.882148
Murray KD, Lohman RB, Bekaert DPS (2021) Cluster-based empirical tropospheric corrections applied to InSAR time series analysis. IEEE Trans Geosci Remote Sens 59:2204–2212. https://doi.org/10.1109/TGRS.2020.3003271
Murray KD, Lohman RB (2018) Short-lived pause in Central California subsidence after heavy winter precipitation of 2017. Sci Adv. https://doi.org/10.1126/sciadv.aar8144
Ohta Y, Ohzono M, Miura S, Iinuma T, Tachibana K, Takatsuka K, Miyao K, Sato T, Umino N (2008) Coseismic fault model of the 2008 Iwate-Miyagi Nairiku earthquake deduced by a dense GPS network. Earth Planets Space 60:1197–1201. https://doi.org/10.1186/BF03352878
Okada T, Umino N, Hasegawa A (2010) Deep structure of the Ou mountain range strain concentration zone and the focal area of the 2008 Iwate-Miyagi Nairiku earthquake, NE Japan—seismogenesis related with magma and crustal fluid. Earth Planets Space 62:347–352. https://doi.org/10.5047/eps.2009.11.005
Ozawa T, Fujita E, Ueda H (2016) Crustal deformation associated with the 2016 Kumamoto Earthquake and its effect on the magma system of Aso volcano. Earth Planets Space 68:1–15. https://doi.org/10.1186/s40623-016-0563-5
Ozawa T, Aoki Y, Okuyama S, Wang X, Miyagi Y, Nohmi A (2019) Database of crustal deformation observed by SAR: improving atmospheric delay mitigation for satellite SAR interferometry and developing L-band multi-type portable SAR. J Disaster Res 14:713–727. https://doi.org/10.2096/jdr.2019.p0713
Pi X, Freeman A, Chapman B, Rosen P, Li Z (2011) Imaging ionospheric inhomogeneities using spaceborne synthetic aperture radar. J Geophys Res. https://doi.org/10.1029/2010JA016267
Shamshiri R, Motagh M, Nahavandchi H, Haghighi MH, Hoseini M (2020) Improving tropospheric corrections on large-scale Sentinel-1 interferograms using a machine learning approach for integration with GNSS-derived zenith total delay (ZTD). Remote Sens Environ 239:111608. https://doi.org/10.1016/j.rse.2019.111608
Shehaj E, Wilgan K, Frey O, Geiger A (2020) A collocation framework to retrieve tropospheric delays from a combination of GNSS and InSAR. Navigation 67:823–842. https://doi.org/10.1002/navi.398
Smith EK, Weintraub S (1953) The constants in the equation for atmospheric refractive index at radio frequencies. Proc IRE 41:1035–1037. https://doi.org/10.1109/JRPROC.1953.274297
Stephens KJ, Wauthier C, Bussard RC, Higgins M, Lafemina PC (2020) Assessment of Mitigation Strategies for Tropospheric Phase Contributions to InSAR Time-Series Datasets over Two Nicaraguan Volcanoes. Remote Sensing 12:782. https://doi.org/10.3390/rs12050782
Takada Y, Sagiya T, Nishimura T (2018) Interseismic crustal deformation in and around the Atotsugawa fault system, central Japan, detected by InSAR and GNSS. Earth Planets Space 70:32. https://doi.org/10.1186/s40623-018-0801-0
Wang X, Aoki Y (2019) Posteruptive thermoelastic deflation of intruded magma in Usu volcano, Japan, 1992–2017. J Geophys Res 124:335–357. https://doi.org/10.1029/2018jb016729
Wegmüller U, Werner C, Strozzi T, Wiesmann A (2006) Ionospheric electron concentration effects on SAR and INSAR. In: 2006 IEEE International Symposium on Geoscience and Remote Sensing. 3731–3734

Xu C, Zhu S (2019) Temporal and spatial movement characteristics of the Altyn Tagh fault inferred from 21 years of InSAR observations. J Geodesy 93:1147–1160. https://doi.org/10.1007/s00190-019-01232-2

Yu C, Li Z, Penna NT (2018a) Interferometric synthetic aperture radar atmospheric correction using a GPS-based iterative tropospheric decomposition model. Remote Sens Environ 204:109–121. https://doi.org/10.1016/j.rse.2017.10.038

Yu C, Li Z, Penna NT, Crippa P (2018b) Generic atmospheric correction model for interferometric synthetic aperture radar observations. J Geophys Res 123:9202–9222. https://doi.org/10.1029/2017JB015305

Zebker HA, Rosen PA, Hensley S (1997) Atmospheric effects in interferometric synthetic aperture radar surface deformation and topographic maps. J Geophys Res 102:7547–7563. https://doi.org/10.1029/96jb03804

Publisher's Note